Geophysical Journal International

Geophys. J. Int. (2022) **228,** 1724–1730
Advance Access publication 2021 October 25
GJI Geomagnetism, Rock Magnetism and Palaeomagnetism

https://doi.org/10.1093/gji/ggab430

The Besnus transition in 4C pyrrhotite revisited

Andreas U. Gehring [1], Alexander Firlus,[1] Dimitrios Koulialias,[1] Peter G. Weidler[2] and Jörg F. Löffler[1]

[1] *Laboratory of Metal Physics and Technology, Department of Materials, ETH Zurich,* 8093 *Zurich, Switzerland. E-mail: agehring@ethz.ch*
[2] *Institute of Functional Interfaces, Karlsruhe Institute of Technology,* 76131 *Karlsruhe, Germany*

Accepted 2021 October 21. Received 2021 October 15; in original form 2021 July 6

SUMMARY

Ferrimagnetic, monoclinic 4C pyrrhotite (Fe_7S_8) is the only iron sulphide with high relevance for palaeomagnetism and rock magnetism that can be identified in rock materials by its characteristic low-temperature anomaly. Despite its relevance in natural magnetism and the many magnetic studies over the last decades, the physics and the crystallography behind this anomaly, also denoted Besnus transition, is a matter of debate. In this study, we analyse the static and dynamic magnetization associated with the Besnus transition in conjunction with low-temperature structural data of 4C pyrrhotite reported in the literature. The correlation between the Fe–Fe bonds causing spin-orbit coupling and the dynamic magnetic properties show that the magnetic characteristics of the Besnus transition stem from the interaction of two magnetocrystalline anisotropy systems triggered by thermally induced structural changes on an atomic level in monoclinic 4C pyrrhotite. This refutes the widespread view that the Besnus transition is caused by a crystallographic change from monoclinic to triclinic.

Key words: Defects; Magnetic properties; Rock and mineral magnetism.

INTRODUCTION

In palaeomagnetism and rock magnetism, the intrinsic low-temperature magnetic anomaly in magnetite (Fe_3O_4), hematite (Fe_2O_3) and 4C pyrrhotite (ideal formula Fe_7S_8) is a key physical property to identify these minerals, which can carry magnetic information in terrestrial and extraterrestrial rock materials for millions of years (Smith & Fuller 1967; Rochette *et al*. 1990; Nagy *et al*. 2017; O'Brien *et al*. 2020). The physics behind this anomaly in the Fe oxides, known as Verwey or Morin transition, is well resolved, whereas the origin of the anomaly in Fe_7S_8 is still a matter of debate. The Verwey transition of Fe_3O_4 has been shown to be caused by a crystallographic change from cubic to monoclinic at $T \approx 120$ K and the Morin transition of Fe_2O_3 by a spin flop at $T \approx 260$ K (e.g. Walz 2002; Özdemir *et al*. 2008). The low-temperature anomaly in Fe_7S_8 at $T \approx 32$ K (Pauthenet 1952; Besnus & Meyer 1964; Rochette *et al*. 2011), also known as Besnus transition, has been explained by a lowering of the crystallographic symmetry similar to the Verwey transition (Fillion & Rochette 1988; Oddou *et al*. 1992; Wolfers *et al*. 2011; Volk *et al*. 2018; Haines *et al*. 2020). Based on group theoretical crystallographic considerations (Haines *et al*. 2019) and on magnetic torque measurements in $B \approx 0.35$ T (Wolfers *et al*. 2011), a crystallographic change from monoclinic to triclinic was postulated. In the latter study, a key evidence was the occurrence of a fourfold rotational symmetry, which was explained by two easy directions in the basal plane close to 45° and 135° due to changes of the twin-partner distribution associated with the formation of a triclinic 4C pyrrhotite (Wolfers *et al*. 2011). Torque measurements by Koulialias *et al*. (2018a) confirmed the appearance of a fourfold symmetry in $B \approx 0.3$ T below the transition and showed that with increasing applied field the sixfold symmetry becomes more prominent. The simultaneous field-dependent occurrence of a fourfold and sixfold rotational symmetry was alternatively explained by the interaction of two magnetocrystalline anisotropy configurations within the monoclinic 4C pyrrhotite structure (Koulialias *et al*. 2018a). This interpretation is in accordance with powder neutron diffraction (PND) studies, which show that above and below the Besnus transition 4C pyrrhotite can be refined in the monoclinic C2/c space group (Powell *et al*. 2004; Koulialias *et al*. 2018b). With this in mind the question arises if a triclinic 4C pyrrhotite is required to explain the Besnus transition.

The controversy over the Besnus transition in 4C pyrrhotite results mainly from the peculiar structural and magnetic properties (Fig. 1). The monosulphide Fe_7S_8 derives from a NiAs-type structure with Fe atoms in four different sites (Fe1, Fe2, Fe3 and Fe4), occupying octahedral interstices of hexagonal close-packed sulphur atoms. Every eighth Fe-site is vacant and this in turn results in the monoclinic 4C pyrrhotite superstructure with a fourfold modulated stacking sequence of full and vacancy layers along the *c*-axis (Bertaut 1953). The sites in the full layers are attributed to Fe1 and Fe3 and those in the vacancy layers to Fe2 and Fe4, where the Fe4-sites are only half-occupied, and their arrangement entails a Kagomé-like sublattice (Fig. 1). The 4C superstructure can be described in the monoclinic space groups F2/d (Tokonami *et al*. 1972)

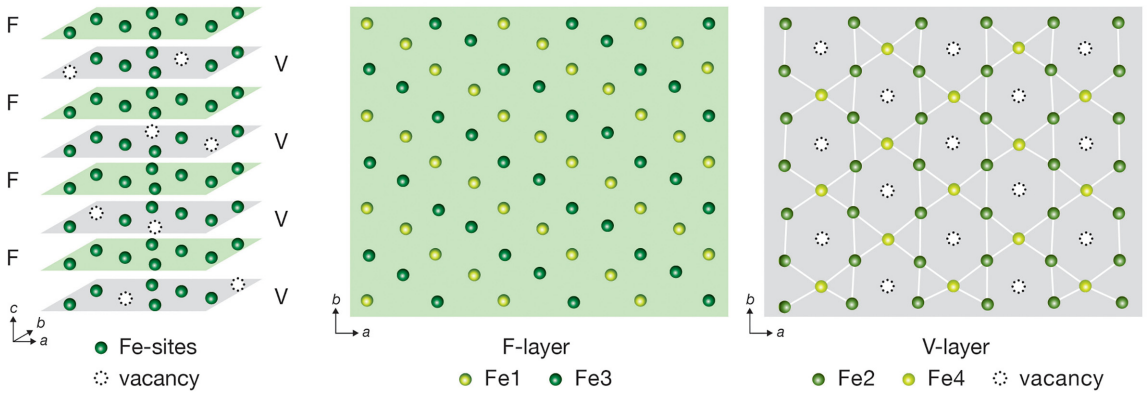

Figure 1. Left: stacking sequence of 4C pyrrhotite (sulphur atoms omitted for clarity) with full (F) and vacancy (V) layers. Middle: view perpendicular to a F-layer with alternating Fe1 and Fe3 sites in rows parallel to the *a*- and *b*-axes. Right: view on the V-layer forming a Kagomé-like sublattice with alternating rows of Fe2 and Fe4 sites parallel to the *a*- and *b*-axes, where one half of the Fe4-sites is vacant.

or C2/c (Powell *et al*. 2004). Moreover, 60° twinning perpendicular to the *c*-axis is a prominent feature often observed in 4C pyrrhotite (Van Landuyt & Amelinckx 1972; Pósfai *et al*. 2000; Jin *et al*. 2021).

The ferrimagnetism of Fe_7S_8 stems from uncompensated sublattices of ferromagnetically coupled intralayer $Fe^{(II)}$ spins and their antiferromagnetic interlayer coupling (Néel 1953; Wang & Salveson 2005; Letard *et al*. 2007). Moreover, 4C pyrrhotite has a distinct magnetocrystalline anisotropy with an easy *c*-plane and a hard *c*-axis, which is manifested by an out-of-plane spin rotation at $T < 200$ K (Weiss 1899; Bin & Pauthenet 1963; Powell *et al*. 2004). The anisotropy is caused by the orbital overlap of Fe–Fe bonds with lengths of less than 3 Å, which generates a pronounced spin-orbit coupling (SOC) between adjacent sublattices (Goodenough 1963; Nesbitt *et al*. 2002). Considering the stacking of the full and vacancy sublattices the Fe-sites can be subdivided into two groups, one (Fe2, Fe3, Fe4) with and the other one (Fe1) without interlayer vacancies as next neighbour (Fig. 1). This arrangement generates two inherently hexagonal site arrangements in the *c*-plane displaced by an angle of 30° (Koulialias *et al*. 2018a). Based on theoretical considerations Adachi (1963) postulated that the Fe-sites of the two groups differ in their local anisotropy. Using Adachi's phenomenological statement in conjunction with an experimental and numerical approach, Koulialias *et al*. (2018c) in fact found two different out-of-plane spin rotations with the polar angles ϑ_I and ϑ_{II} that could be attributed to the two groups. Given this, 4C pyrrhotite can be seen as a magnetic system with two anisotropy components.

Numerous magnetic studies in the last decades fostered different interpretations of the Besnus transition, but their critical evaluation with structural data is generally fragmentary. Here we present a low-temperature static and dynamic magnetization study of a well characterized, natural, pure-phase 4C pyrrhotite and correlate it with structural data from the literature. The results are then discussed in the context of different explanations presented for the Besnus transition.

MATERIAL AND METHODS

A 4C pyrrhotite crystal from the Morro Velho gold mine in Brazil (Vial *et al*. 2007) was used. The structural and magnetic properties of samples from this locality have been extensively studied over more than a century (e.g. Weiss 1905; Buerger 1947; Volk *et al*. 2016; Koulialias *et al*. 2018b, 2019; Haines *et al*. 2020). For structural analysis we took the powder X-ray diffraction data at 300 K and the powder neutron diffraction (PND) data set published by Koulialias *et al*. (2018b), which were obtained from a sister sample of the crystal used in this study.

All static and dynamic magnetic measurements of this multidomain 4C pyrrhotite between 5 and 300 K were performed in the easy *c*-plane on a MPMS3 SQUID magnetometer using the vibrating sample magnetometer (VSM) or the alternating current (AC) option. The static magnetization was analysed by field-cooling experiments in fields between 0.1 and 3 T from 300 K down to 5 K and by hysteresis measurements at selected temperatures. The latter measurements were performed after demagnetization of the sample at 300 K and cooling it in a zero-field. Furthermore, dynamic magnetic properties associated with the Besnus transition were examined by frequency-dependent AC susceptibility measurements with an amplitude of 1 mT and a parallel 0.1 T direct current (DC) bias field, in a range of 5–200 Hz at 0.05 K temperature steps.

RESULTS AND DISCUSSION

Structural properties

The Morro Velho 4C pyrrhotite is a pure-phase crystal with unit cell parameters $a = 11.9140 \pm 0.0004$ Å, $b = 6.8711 \pm 0.0003$ Å, $c = 12.9082 \pm 0.0005$ Å and $\beta = 118.0517 \pm 0.0013°$ at 300 K (Koulialias *et al*. 2018b). For the primitive hexagonal NiAs-like substructure (P63/mmc) unit cell parameters of $a = b = 3.4371 \pm 0.0003$ Å and $c = 5.6977 \pm 0.0007$ Å were calculated and they are similar to those reported by Fillion *et al*. (1992). In contrast to the numerous X-ray diffraction studies at 300 K, there is only little crystallographic information on Fe_7S_8 at low temperature, which was generally obtained from neutron diffraction studies (Fillion *et al*. 1992; Powell *et al*. 2004; Wolfers *et al*. 2011; Koulialias *et al*. 2018b). In two of these studies, PND patterns above and below the Besnus transition were refined in the monoclinic C2/c space group (Powell *et al*. 2004; Koulialias *et al*. 2018b). Haines *et al*. (2020) used the unit cell parameters from these PND studies and determined symmetry-breaking shear strains given by $(a–b)/((ab)^{1/2})$ and $\cos\beta*$, where $\beta*$ is the reciprocal lattice angle β of the 4C pyrrhotite in the monoclinic F2/d space group. They inferred that one of the monoclinic angles changes from 90° to $\leq \sim 90.06°$. Such a departure is, however, too little to

unambiguously support symmetry lowering at the Besnus transition, also considering that Tokonami *et al*. (1972) found an angle β of 90.43° for 4C pyrrhotite at 300 K. Nevertheless, we use here the PND data by Koulialias *et al*. (2018b) for a detailed inspection in a wide *d*-spacing range in order to evaluate the possibility of a crystallographic change at low temperature (Fig. 2). The *d*-spacing range is critically affected by extinction rules that in turn depend on the mineral's space group. For monoclinic 4C pyrrhotite, the $(\bar{1}11)$ crystallographic peak has the highest spacing with $d = 5.71$ Å and it is superimposed by the strongest magnetic peak (Powell *et al*. 2004; Koulialias *et al*. 2018b). An additional weak peak at $d \approx 6.7$ Å in the PND pattern may be attributed to (010) in a triclinic $P\bar{1}$ structure or to a magnetic peak (Fig. 2). Because this single peak is detectable over the whole temperature range a triclinic 4C pyrrhotite can be excluded. Given this and considering the minor release of shear strain at the Besnus transition, as reported by Haines *et al*. (2020), the structural changes in monoclinic 4C pyrrhotite at low temperature must be on the atomic level.

The unit cell parameters *a* and *c* of the hexagonal substructure (Fillion *et al*. 1992) and *a*, *b* and *c* of the monoclinic superstructure (Koulialias *et al*. 2018b) continuously decrease upon cooling to about 50 K and exhibit little changes at lower temperature. It is worth noting that the thermal contraction is anisotropic with a slight expansion in *b* direction at $T < 50$ K. Simultaneously, the angles of the six Fe–S–Fe super-exchange paths in 4C pyrrhotite become more regular upon cooling and tend towards 135° (Koulialias *et al*. 2018b). Such a value is characteristic of an undistorted NiAs-type structure with antiferromagnetic interactions (Goodenough 1963). With this in mind the change towards an angle of 135° within the 4C pyrrhotite lattice suggests a decrease in distortion and subsequently a release of shear strain associated with the Besnus transition. It is worth noting that for a Morro Velho 4C pyrrhotite sample such release coincides with a peak in the heat capacity (Volk *et al*. 2018; Haines *et al*. 2020).

Thermal contraction also affects the Fe–Fe bond lengths, which again determine the SOC, that is the magnetocrystalline anisotropy. At low temperature four Fe–Fe bonds with lengths of less than 3 Å contribute to the SOC of 4C pyrrhotite (Fig. 3). Three of them are interlayer bonds and one is an intra-layer bond. Moreover, the Fe3-sites are those with no vacancy as next neighbour, and therefore they have lesser freedom to be yielded by stress/strain in the crystallographic lattice (Fig. 1). The structural changes that affect the anisotropic properties in the 4C pyrrhotite are best manifested in the Fe3–Fe2 and Fe3–Fe4 bond lengths, which converge in conjunction with the Besnus transition (Fig. 3).

Magnetic properties

At 300 K a field of $B = 2$ T in the *c*-plane results in a magnetization $M_{2T} = 21.2$ Am^2 kg^{-1} (Fig. 4), which is near the theoretical value for 4C pyrrhotite estimated by Néel (1953). Saturation, however, is not reached due to slight spin tilting, which is caused by the high anisotropy field of about 13 T at 300 K (Koulialias *et al*. 2018c). Upon cooling the M_{2T} curve reveals a concave shape between 300 K and 50 K followed by a discontinuity indicating the low-temperature transition. The field-cooled magnetization is implicitly related to the total free energy of the system (E_{tot}), given as the superposition of the Zeeman (E_Z) and the magnetocrystalline anisotropy (E_{an}) energy contributions: $E_{tot} = E_z + E_{an}$. The temperature-dependent quantities that enter this equation are the magnetocrystalline anisotropy constants within E_{an} and the absolute value of the net magnetization vector within E_Z. Considering the work of Bin & Pauthenet (1963), the absolute value of the magnetization exhibits a steady increase of about 3 per cent between 300 and 150 K and becomes nearly constant at lower temperature, whereas at $T < 200$ K the change in sign of one of the three magnetocrystalline anisotropy constants (K_3) leads to a gradual out-of-plane spin rotation, which was experimentally confirmed by PND studies (Powell *et al*. 2004; Koulialias *et al*. 2018b). The onset of the gradual spin rotation coincides with the drop of the intra-layer Fe3–Fe3 bond lengths below the critical value of 3 Å and this in turn indicates an additional contribution to the overall SOC in 4C pyrrhotite (Koulialias *et al*. 2018b). Taking the above, the thermal behaviour of M_{2T} mirrors the interplay between E_Z and E_{an}, and the maximum in the field-cooled magnetization curve at $T \approx 170$ K marks the onset of a prevailing contribution of E_{an} (Fig. 4). This effect is also seen at lower fields in the $M_{0.1T}$ curve. Both the M_{2T} and $M_{0.1T}$ curves can be described with a second-order polynomial fit down to $T \approx 50$ K, and this in turn suggests that the concave shapes are critically affected by the out-of-plane spin rotation (Fig. 4). The shallowing with a local minimum at $T = 44$ K marks the change in the spin rotation regime with respect to the (001) plane of the 4C pyrrhotite. This temperature accords with the onset of a pronounced SOC change, as indicated by the Fe3–Fe2 and Fe3–Fe4 bonds (Fig. 3). Theoretically, the spin rotation has two degrees of freedom, parallel to the (001) plane and in/out of the easy plane. It can be assumed that in a 2 T field the spins are aligned in the *c*-plane and the effects of domains and twins are negligible. Based on this the spins of the two groups of Fe-sites only differ in the polar angles ϑ_I and ϑ_{II} and the increase in M_{2T} associated with the Besnus transition is caused by the reversed in-plane rotation of the angle ϑ_{II} (Koulialias *et al*. 2018c). The peak in the M_{2T} curve then indicates the minimum in ϑ_{II} and the return to coherent out-of-plane spin rotations in the two groups at lower temperature. The relative increase in the magnetization curves in the temperature range between 44 K and 31 K is field-dependent with 1.4 per cent in M_{2T} and 17.9 per cent in $M_{0.1T}$, respectively. Because of the hard uniaxial anisotropy, the more pronounced jump in the $B = 0.1$ T field points to prevailing azimuthal spin rotation in the easy plane due to a change in the SOC. Considering the fourfold symmetry in the in-plane torque experiments in relatively low fields (Wolfers *et al*. 2011; Koulialias *et al*. 2018a), the jump in $M_{0.1T}$ can mainly be attributed to an interaction onset of the two anisotropy systems in 4C pyrrhotite. With this in mind the field-dependent magnetization jump associated with the Besnus transition reveals the formation of a system with interacting anisotropies that are dominated by the uniaxiality of the 4C pyrrhotite.

Fig. 5 shows the in-phase χ' and the out-of-phase χ'' susceptibility in a 0.1 T DC bias field. The in-phase, which mirrors the slope of the field-cooled magnetization curve, shows at $T = 31.5$ K a peak with a weak frequency dependence on the low-temperature side (Fig. 5a). The out-of-phase susceptibility is indicative of dissipative processes and reveals changes in a range of about 10 K flanking the Besnus transition, with two local maxima at 34 K and 30 K and a local minimum at $T \approx 31.5$ K (Fig. 5b). The latter two exhibit a frequency dependence. At low frequency, the minimum is associated with a shoulder and with increasing frequency the two features merge to a relatively flat one (Fig. 5b). This conversion in χ'' at $T \approx 31.5$ K coincides with the maximum in χ', a peak in the heat capacity of a Moro Velho pyrrhotite (Volk *et al*. 2018), and with a distortion decrease in the NiAs-like substructure (Koulialias *et al*. 2018b). With this in mind the frequency dependence of χ'' at $T \approx 31.5$ K is most likely a dissipative effect due to the change from incoherent to coherent spin rotation and the interaction onset of the

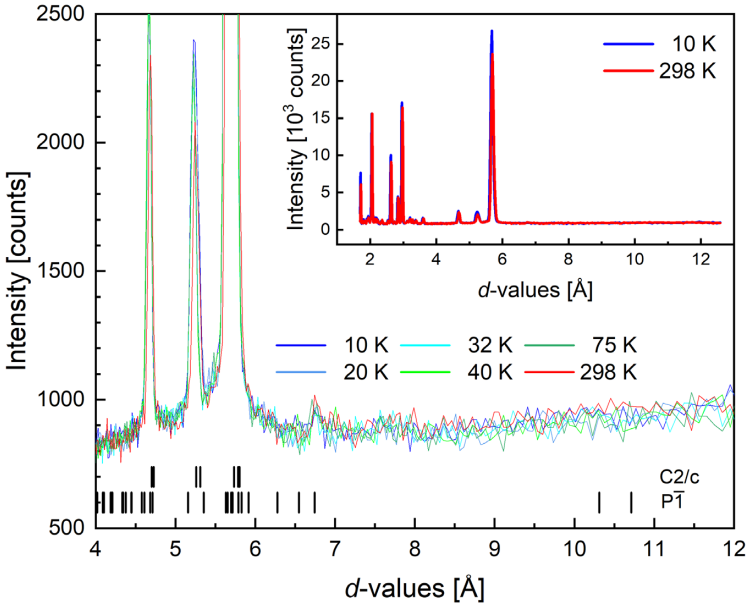

Figure 2. Wide *d*-spacing range of the PND patterns in the temperature range between 10 and 298 K, with the diffraction peak positions in monoclinic C2/c and triclinic Pff space groups marked. The inset shows the whole range of the PND pattern at 298 and 10 K, where the strongest peak is due to (002) magnetic diffraction.

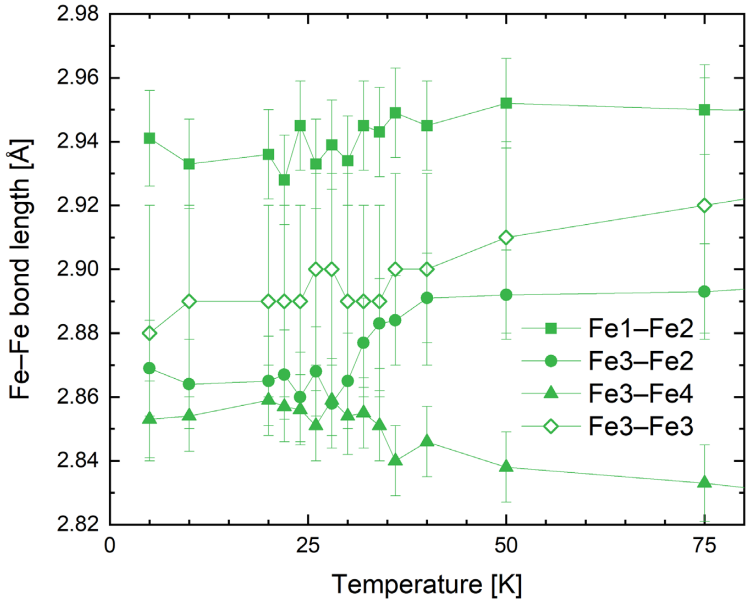

Figure 3. Fe–Fe bond lengths of less than 3 Å in 4C pyrrhotite, from Koulialias *et al*. (2018b). Full symbols represent interlayer and open symbols represent intralayer Fe–Fe bonds.

two anisotropy systems at the Besnus transition. Moreover, the peak at $T = 30$ K, which can be regarded as the lower limit of the scope of the transition manifested in $B = 0.1$ T (Fig. 4, inset), exhibits a shift to higher temperature with increasing frequency f. Taking the Arrhenius-Néel equation $f(T) = f_0 \exp(-\Delta E/k_B T)$ into account, where f is the excitation frequency, f_0 is the attempt frequency, ΔE is the energy barrier, k_B is the Boltzmann constant and T is the temperature, an activation energy $\Delta E = 1.7$ eV (2.72×10^{-19} Joule) is obtained from the f versus $1/T$ plot (Fig. 5c). Considering the energy levels of the Fe orbitals in pyrrhotite (Sakkopoulos *et al*. 1984; Nesbitt *et al*. 2002), such ΔE can be assigned to changes in the spin structure and the electron correlation, respectively, presumably due to a coupling of itinerant spins to localized spins. Evidence for such a change in 4C pyrrhotite is a decrease in resistivity (Besnus & Meyer 1964), an electronic contribution to the specific heat (Kobayashi *et al*. 1999), and higher-order terms in the anisotropic magnetic resistivity (Charilaou *et al*. 2015).

Above the Besnus transition the hysteresis loops recorded in the basal plane show the typical properties of a multidomain 4C pyrrhotite (e.g. Dekkers *et al*. 1989; Volk *et al*. 2016). The hysteresis parameters at 300 K are coercivity $B_c = 1.9$ mT, magnetization at 3 T field $M_{3T} = 21.4$ Am^2 kg^{-1}, remanence magnetization $M_r = 1.0$ Am^2 kg^{-1}, and a squareness ratio $M_r/M_{3T} = 0.05$. At $T = 50$ K, the parameters are nearly the same, but the hysteresis curve exhibits

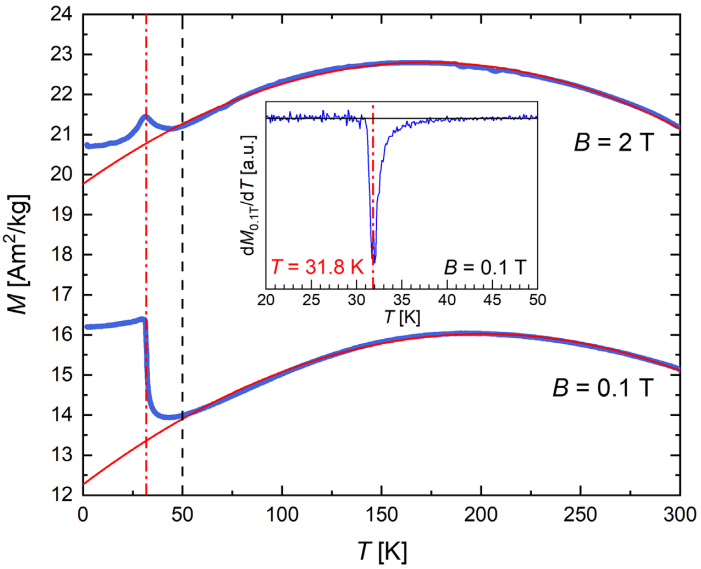

Figure 4. Field-cooling magnetization curves, where the dashed black line marks the lower limit of the polynomial fitting (red). The dash-dotted red line marks the inflection point in the $B = 0.1$ T differential curve (inset) and the local maximum in the $B = 2$ T curve.

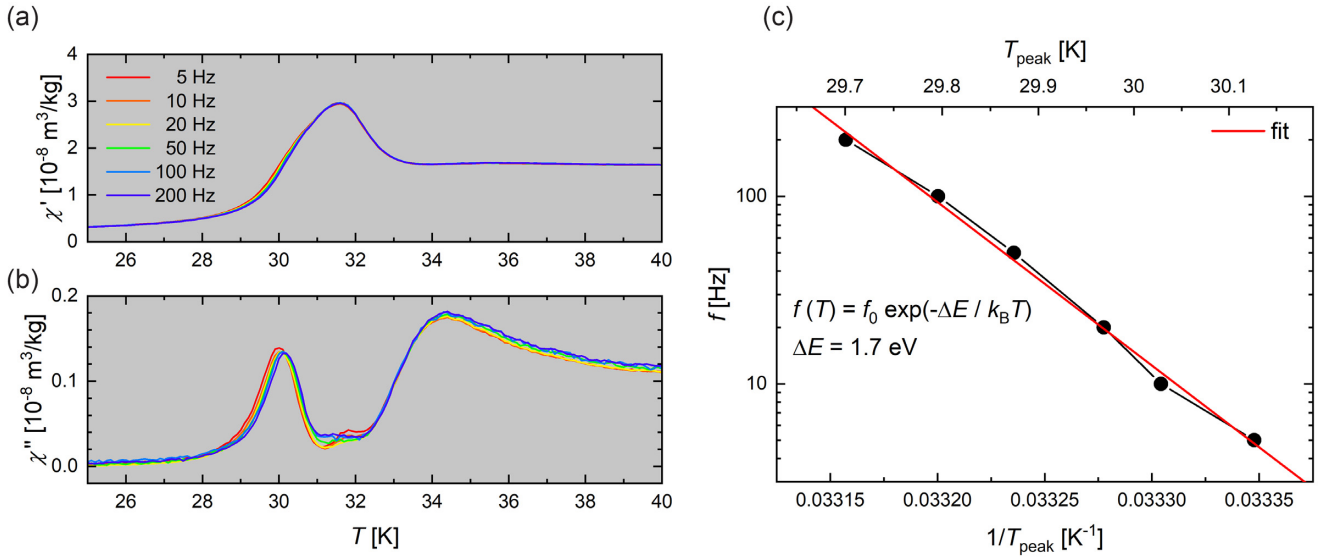

Figure 5. Highly resolved AC susceptibility with an amplitude of 1 mT and a parallel DC bias field of 0.1 T in a frequency range between 5 and 200 Hz: (a) the in-phase signal χ' shows a weak frequency dependence at around 30 K and (b) the out-of-phase signal χ'' reveals a frequency dependence at $T \approx 31.5$ and 30 K, respectively. (c) Arrhenius–Néel plot of the frequency dependence of χ'' at 30 K (peak of χ'' in panel b).

the characteristic second inflection (Fig. 6a) that was first described by Koulialias *et al*. (2016). Volk *et al*. (2016) demonstrated that this effect has an angular dependence and is most pronounced if the external field has a 30° angle to the *a*-axis of the 4C pyrrhotite. These authors interpreted the second inflection as a field-induced easy axis flipping. Based on crystallographic considerations, Koulialias *et al*. (2018a), however, explained this hysteresis effect as a response of two superimposed, hexagonal anisotropy systems caused by the vacancy order in the stacking sequence of full and Kagomé-like sublattices (Figs 1b and c). The easy *c*-plane exhibits a sixfold rotational symmetry as it is expected for the hexagonal NiAs-type substructure (Koulialias *et al*. 2016; Volk *et al*. 2016). Given this, the two anisotropy systems inferred by Koulialias *et al*. (2018a) must also have a sixfold rotation symmetry with no interactions.

Below the Besnus transition the second inflection vanishes again (Fig. 6b). Associated with this transition, the appearance of a fourfold rotational symmetry has been reported (Volk *et al*. 2018; Koulialias *et al*. 2018a). Taking the structural properties of the monoclinic 4C pyrrhotite into account, this fourfold symmetry points to an interaction of the two hexagonal anisotropy systems displaced by 30°. The simultaneous increase of the hysteresis parameters in the multidomain 4C pyrrhotite, with $B_c = 135.3$ mT and $M_r/M_{3T} = 0.8$ at 10 K (Fig. 6b), is then most likely caused by a gain in domain-wall (DW) energy triggered by the interacting anisotropy systems, that is the remagnetization becomes harder. Moreover, the magnetization of the initial curve at 10 K is somewhat lagged with a nearly zero increase up to 50 mT (Fig. 6b, inset). This 50 mT field can be taken as a measure for the energy barrier to be overcome in order to initiate DW movement. With this in mind the characteristic

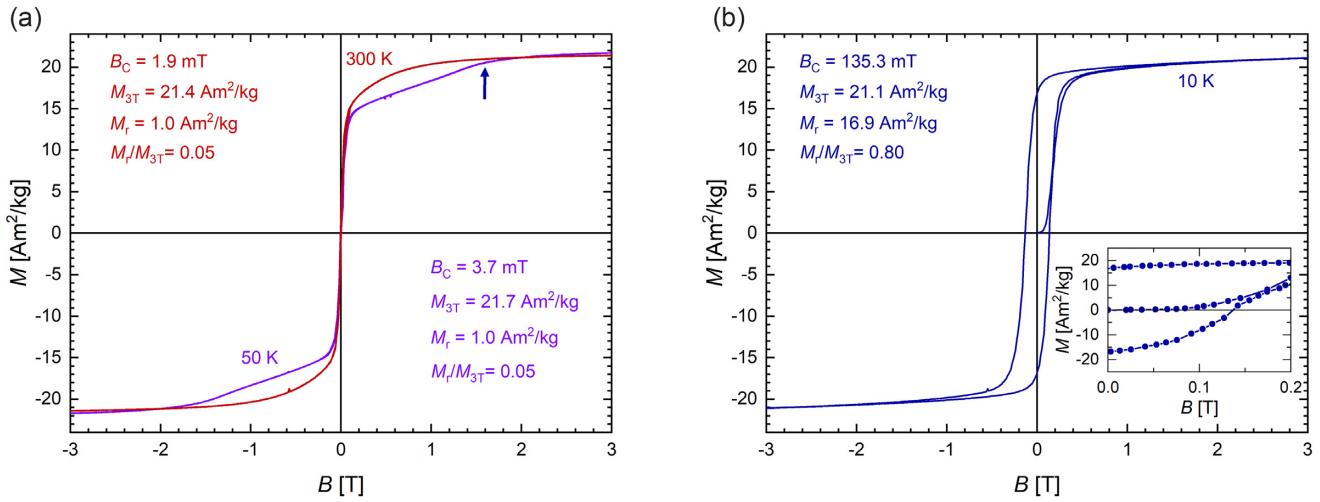

Figure 6. (a) Hysteresis curves at 300 K (red) and at 50 K (violet) with the latter showing a second inflection (see arrow). (b) Hysteresis and initial curve at 10 K, where the second inflection has vanished again. Inset: narrow range of the hysteresis, revealing that the initial curve has nearly zero magnetization up to 50 mT.

increase in the hysteresis parameters below the Besnus transition (e.g. Dekkers *et al*. 1989; Charilaou *et al*. 2015; Volk *et al*. 2016.) can be explained by the growth of the DW thickness due to the interacting magnetocrystalline anisotropy systems. Such change of the DW properties in multidomain 4C pyrrhotite accords well with the loss of the amplitude dependence in AC susceptibility below the Besnus transition (Kind *et al*. 2013).

SUMMARY AND CONCLUSIONS

The powder neutron diffraction data by Koulialias *et al*. (2018b) provide no evidence for a monoclinic to triclinic symmetry change associated with the Besnus transition. The change of the monoclinic angle β from 90° to $\leq$ ~90.06°, as calculated by Haines *et al*. (2020) from these diffraction data, may indicate a lowering of the crystallographic symmetry below the Besnus transition. The analysis of the structural properties in the temperature range between 298 and 10 K, however, reveals a different picture. Thermal contraction associated with the Besnus transition leads to a more regular NiAs-like substructure and this in turn suggests that the distortion in the 4C superstructure decreases.

In fact, the very minor departure of the monoclinic angle β reported by Haines *et al*. (2020) can be explained by structural changes on an atomic level within the C2/c space group. Such change governs the variation of the Fe–Fe bonds with lengths of less than 3 Å, which critically affect the spin-orbit coupling in NiAs-like structures and therefore the magnetocrystalline anisotropy in 4C pyrrhotite. The highly ordered vacancies in the 4C superstructure generate two anisotropy systems, where the onset of their interactions marks the Besnus transition and can explain the changes in the magnetic properties at low temperature. In conclusion, the magnetic anomaly of the Besnus transition stems from the magnetocrystalline anisotropy of a crystal structure with ordered vacancies in a Kagomé-like Fe sublattice, which is a characteristic trait of monoclinic 4C pyrrhotite.

ACKNOWLEDGEMENTS

The authors thank Mark Dekkers and an anonymous reviewer for their comments. This work was supported by an ETH Research Grant (ETH-47 17-1).

DATA AVAILABILITY

The data underlying this paper will be shared on reasonable request to the corresponding author.

REFERENCES

Adachi, K., 1963. Origine de l'énergie d'anisotropie magnétocristalline de la pyrrhotine, *J. Phys.,* **24,** 725–731.

Bertaut, E.F., 1953. Contribution à l'étude des structures lacunaires: la pyrrhotine, *Acta. Crystallogr.,* **6,** 557–561.

Besnus, M. J. & Meyer, A.J.P., 1964. Nouvelles données expérimentales sur le magnétisme de la pyrrhotine naturelle, in *Proceedings of Int. Conf. Mag.,* Nottingham, pp. 507–511.

Bin, M. & Pauthenet, R., 1963. Magnetic anisotropy in pyrrhotite, *J. Appl. Phys.,* **34,** 1161.

Buerger, M.J., 1947. The cell and symmetry of pyrrhotite, *Am. Mineral.,* **32,** 411–414.

Charilaou, M., Kind, J., Koulialias, D., Weidler, P.G., Mensing, C., Löffler, J.F. & Gehring, A.U., 2015. Magnetic-electronic coupling in modulated defect-structures of natural $Fe_{1-x}S$, *J. Appl. Phys.,* **118,** 083903.

Dekkers, M.J., Mattéi, J.-L., Fillion, G. & Rochette, P., 1989. Grain-size dependence of the magnetic behavior of pyrrhotite during its low-temperature transition at 34 K, *Geophys. Res. Lett.,* **16,** 855–858.

Fillion, G. & Rochette., R., 1988. The low temperature transition in monoclinic pyrrhotite, *J. Phys. Colloq.,* **49,** 907–908.

Fillion, G., Mattéi, J., Rochette, P. & Wolfers, P., 1992. Neutron study of 4C pyrrhotite, *J. Magn. Magn Mater.,* **104–107,** 1985–1986.

Goodenough, J. B., 1963. *Magnetism and the Chemical Bond,* Interscience (Wiley).

Haines, C.R.S., Howard, C.J., Harrison., R.J. & Carpenter, M.A., 2019. Group-theoretical analysis of structural instability, vacancy ordering and magnetic transitions in the system troillite (FeS)-pyrrhotite ($Fe_{1-x}S$), *Acta. Crystallogr.,* **875,** 1208–1224.

Haines, C.R.S., Dutton, S.E., Volk, M.W.R. & Carpenter, M.A., 2020. Magnetoelastic properties and behaviour of 4C pyrrhotite, Fe_7S_8, through the Besnus transition, *J. Phys.: Condens. Matter,* **32,** 405401.

Jin, L. *et al.*, 2021. Atomic-scale characterization of commensurate and incommensurate vacancy superstructures in natural pyrrhotites, *Am. Mineral.,* **106,** 82–96.

Kind, J., García-Rubio, I., Charilaou, M., Nowaczyk, N.R., Löffler, J.F. & Gehring, A.U., 2013. Domain-wall dynamics in 4C pyrrhotite at low temperature, *Geophys. J. Int.,* **195,** 192–199.

Kobayashi, H., Nozue, T., Matsumura, T., Suzuki, T. & Kamimura, T., 1999. The low-temperature specific heat of FeS and $M_{0.875}X$ (M = Fe, Co; X = S, Se) with a NiAs-like structure, *J. Phys.: Condens. Matter,* **11,** 8673–8679.

Koulialias, D., Kind, J., Charilaou, M., Weidler, P.G., Löffler, J.F. & Gehring, A.U., 2016. Variable defect structures cause the magnetic low-temperature transition in natural monoclinic pyrrhotite, *Geophys. J. Int.,* **204,** 961–967.

Koulialias, D., Charilaou, M., Schäublin, R., Mensing, C., Weidler, P.G., Löffler, J.F. & Gehring, A.U., 2018a. Ordered defects in $Fe_{1-x}S$ generate additional magnetic anisotropy symmetries, *J. Appl. Phys.,* **123,** 033902.

Koulialias, D., Canévet, E., Charilaou, M., Weidler, P.G., Löffler, J.F. & Gehring, A.U., 2018b. [1]The relation between local structural distortion and the low-temperature magnetic anomaly in Fe_7S_8, *J. Phys.: Condens. Matter,* **30,** 425803.

Koulialias, D., Charilaou, M., Mensing, C., Löffler, J.F. & Gehring, A.U., 2018c. Torque analysis of incoherent spin rotation in the presence of ordered defects, *Appl. Phys. Lett.,* **112,** 202404.

Koulialias, D., Weidler, P.G., Charilaou, M., Löffler, J.F. & Gehring, A.U., 2019. Cation diffusion patterns across the magneto-structural transition in Fe_7S_8, *Phys. Chem. Chem. Phys.,* **21,** 13 040–13 046.

Letard, I., Sainctavit, P. & Deudon, C.(2007). XMCD at Fe $L_{2,3}$ edges, Fe and S K edges on Fe_7S_8, *Phys. Chem. Miner.,* **34,** 113–120.

Nagy, L., Williams, W., Muxworthy, A.R., Fabian, K., Almeidad, T.P., Conbhuía, P. Ó. & Shcherbakov, V., 2017. Stability of equidimensional pseudo–single-domain magnetite over billion-year timescales, *Proc. Natl. Acad. Sci. USA,* **114,** 10356–10360.

Néel, L., 1953. Some new results on antiferromagnetism and ferromagnetism, *Rev. Mod. Phys.,* **25,** 58–63.

Nesbitt, H.W., Schaufuss, A.G., Bancroft, G.M. & Szargan, R., 2002. Crystal orbital contributions to the pyrrhotite valence band with XPS evidence for weak Fe–Fe π bond formation, *Phys. Chem. Miner.,* **29,** 72–77.

O'Brien, T., Tarduno, J.A., Anand, A., Smirnov, A.V., Blackman, E.G., Carroll-Nellenback, J. & Krot, A.N., 2020. Arrival and magnetization of carbonaceous chondrites in asteroid belt before 4562 million years ago, *Commun. Earth Environ.,* **1,** 54.

Oddou, J.L., Jeandey, C., Mattéi, J. L. & Fillion, G., 1992. Mössbauer study of the low-temperature transition in pyrrhotite, *J. Magn. Magn. Mater.,* **104,** 1987–1988.

Özdemir, Ö., Dunlop, D.J. & Berquó, T.S., 2008. Morin transition in hematite: size dependence and thermal hysteresis, *Geochem. Geophys. Geosyst.,* **9,** Q10Z01, doi:10.1029/2008GC002110.

Pauthenet, R., 1952. Etude magneétique d'un monocristal de pyrrhotine aux basses températures, *C. R. Acad. Sci., Paris,* **234,** 2261–2263.

Pósfai, M., Sharp, T.G. & Kontny, A., 2000. Pyrrhotite varieties from the 9.1 km deep borehole of the KTB project, *Am. Mineral.,* **85,** 1406–1415.

Powell, A.V., Vaqueiro, P., Knight, K.S., Chapon, L.C. & Sánchez, R.D., 2004. Structure and magnetism in synthetic pyrrhotite Fe_7S_8: a powder neutron-diffraction study, *Phys. Rev. B,* **70,** 014415.

Rochette, P., Fillion, G., Mattéi, J.L. & Dekkers, M.J., 1990. Magnetic transition at 30–34 Kelvin in pyrrhotite: insight into a widespread occurrence of this mineral in rocks, *Earth planet. Sci. Lett.,* **98,** 319–328.

Rochette, P., Fillion, G. & Dekkers, M. J. 2011. Interpretation of low-temperature data part 4: the low-temperature magnetic transition of monoclinic pyrrhotite, *IRM Q.,* **21,** 1–11.

Sakkopoulos, S., Vitoratos, E. & Argyreas, T., 1984. Energy-band diagram for pyrrhotite, *J. Phys. Chem. Solids,* **45,** 923–928.

Smith, R.W. & Fuller, M., 1967. Alpha-hematite: stable remanence and memory, *Science,* **156,** 1130–1133.

Tokonami, M., Nishiguchi, K. & Morimoto, N., 1972. Crystal structure of a monoclinic pyrrhotite (Fe_7S_8), *Am. Mineral.,* **57,** 1066–1080.

Van Landuyt, J. & Amelinckx, S., 1972. Electron microscope observations of the defect structure of pyrrhotite, *Mater. Res. Bull.,* **7,** 71–79.

Vial, D.S., DeWitt, E., Lobato, L.M. & Thorman, C.H., 2007. The geology of the Morro Velho gold deposit in the Archean Rio das Velhas greenstone belt, Quadrilátero Ferríferro, Brazil, *Ore Geol. Rev.,* **32,** 511–542.

Volk, M.W.R., Gilder, S.A. & Feinberg, J.M., 2016. Low-temperature magnetic properties of monoclinic pyrrhotite with particular relevance to the Besnus transition, *Geophys. J. Int.,* **207,** 1783–1795.

Volk, M.W.R., McCalla, E, Voigt, B, Manno, M., Leighton, C. & Feinberg, J.M., 2018. Changes in properties of 4C pyrrhotite (Fe_7S_8) across the 32 K Besnus transition, *Am. Mineral.,* **103,** 1674–1689.

Walz, F., 2002. The Verwey transition—a topical review, *J. Phys: Condens. Matter,* **14**. 285–340.

Wang, H. & Salveson, I., 2005. A review on the mineral chemistry of the non-stoichiometric iron sulphide, $Fe_{1-x}S$ ($0 \leq x \leq 0.125$): polymorphs, phase relations and transitions, electronic and magnetic structures, *Phase Trans.,* **78,** 547–567.

Weiss, P., 1899. Sur l'aimantation plane de la pyrrhotine, *J. Phys. Théor. Appl.,* **4,** 469–508.

Weiss, P., 1905. Les propriétés magnétiques de la pyrrhotine, *J. Phys. Théor. Appl.,* **8,** 542–544.

Wolfers, P., Fillion, G., Ouladdiaf, B., Ballou, R. & Rochette, P., 2011. The pyrrhotite 32 K magnetic transition, *Solid State Phenom.,* **170,** 174–179.